Journal of Materials Chemistry A

ROYAL SOCIETY OF CHEMISTRY

PAPER

View Article Online
View Journal | View Issue

Cite this: J. Mater. Chem. A, 2025, 13, 30427

Spectroscopic analysis of Cu^{2+} dissolved in Y- and Yb-doped barium zirconates and its impact on sinterability and proton conduction

Yuto Unaki, [a] Hiroaki Kawamori,[b] Shohei Kobayashi,[b] Norikazu Osada,[b] Akihiro Ishii, [a] Itaru Oikawa[a] and Hitoshi Takamura *[a]

Received 22nd April 2025
Accepted 7th August 2025

DOI: 10.1039/d5ta03169a

rsc.li/materials-a

Y- and Yb-doped barium zirconates are currently the most promising proton conductors for application in fuel cells and electrolyzers. To achieve a high density without sintering at a high temperature of approximately 1600 °C, the addition of sintering aids, such as NiO, CuO, or ZnO, is necessary. However, the sintering mechanism and influence of the incorporation of sintering aids into the lattice on proton conduction remain unclear. In this study, the sintering mechanism was investigated using model experiments with diffusion couples between CuO and $BaCe_{0.4}Zr_{0.4}Y_{0.1}Yb_{0.1}O_{3-\delta}$ (BCZYY441), and the dissolution state of Cu and its effect on proton conduction were analyzed using Raman and ESR spectroscopy. The results revealed that the formation of a liquid phase is crucial for the sintering effect. ESR spectroscopy revealed that the sintering aids dissolved at the interstitial sites adversely affecting the proton conduction, especially the proton transference number. Therefore, processes to remove dissolved sintering aids or explore new sintering aids are necessary.

Introduction

Proton-conducting solid electrolytes have attracted attention for applications in fuel cells and electrolyzers because they can operate at lower temperatures than oxide-ion-conducting electrolytes.[1–5] Since the discovery of $SrCeO_3$ as a proton-conducting perovskite by Iwahara *et al.* in 1981,[6] various proton-conducting materials have been developed.[7–11] Among these, $BaCeO_3$ exhibits high proton conductivity but suffers from decomposition owing to reactions with water vapor and carbon dioxide.[12–14] In contrast, $BaZrO_3$ has excellent chemical stability, and $BaCe_{1-x-y-z}Zr_xY_yYb_zO_{3-\delta}$ has garnered attention for its combination of high proton conductivity and chemical stability.[15–22] Solid electrolytes require high densification to suppress the grain boundary resistance. However, achieving densification in perovskite-type proton conductors requires sintering temperatures above 1600 °C, which poses challenges such as increased manufacturing costs and decreased conductivity owing to the volatilization of Ba and the segregation of doping elements.[23–25] Therefore, low-temperature sintering is highly desirable.

Low-temperature sintering techniques include "spark plasma sintering", hot pressing, and pulsed electric current sintering.[26–28] Recently, laser sintering and backlight sintering have also been investigated as a novel approach.[29–31] However, these methods have limitations in terms of cost, product shape, and size. The addition of sintering aids provides an inexpensive and effective method for pressure-less low-temperature sintering. The sintering promotion mechanism of sintering aids is primarily attributed to either the formation of secondary phases (*i.e.*, liquid or reactive phases) or the creation of a solid solution. The former mechanism involves dissolution of the parent phase into the liquid phase, thereby accelerating densification.[32] For instance, low-melting-point materials such as LiF can act as liquid-phase promoters.[33] The latter mechanism relies on the incorporation of sintering aids into the parent phase, which increases the vacancy concentration and promotes sintering, as observed for WC-doped TiC.[34] Babilo and Haile systematically investigated transition metal oxides ranging from Sc to Zn as sintering aids for perovskite-type proton conductors and found that ZnO, CuO, and NiO particularly enhance sinterability.[25,35,36] However, the detailed mechanisms underlying the promotion of sintering by these aids remain unclear. Nikodemski *et al.* proposed that divalent ions (*i.e.*, Ni^{2+}, Cu^{2+}, Zn^{2+}, Co^{2+}) with ionic radii similar to Zr^{4+} can dissolve into the B-site, creating ionic defects that facilitate diffusion and improve sinterability.[37] Conversely, other studies have reported sinterability enhancement through liquid-phase formation.[38,39] Han *et al.* suggested that the interstitial incorporation of Ni induces Ba segregation at grain boundaries, promoting liquid-phase

[a]Department of Materials Science, Graduate School of Engineering, Tohoku University, 6-6-02 Aramaki Aoba, Sendai 980-8579, Japan. E-mail: takamura@material.tohoku.ac.jp

[b]Energy Systems Research & Development Center, Toshiba Energy Systems & Solutions Corporation, 2-4 Suehiro-cho, Tsurumi-ku, Yokohama-shi, Kanawgawa 230-0045, Japan

formation and improving sinterability.[40] Thus, the consensus on the mechanism of sintering promotion by sintering aids remains elusive.

Furthermore, all studies have reported a reduction in proton conductivity with the addition of sintering aids.[41,42] This decline in proton conductivity is attributed to the reactivity between the sintering aids and parent phase and the incorporation of sintering aids into the lattice. For example, NiO reacted with Y-doped $BaZrO_3$ (BZY) to form BaY_2NiO_5, as reported by Tong *et al.*[43] Similarly, CuO is known to form secondary phases.[44] These reactions may extract acceptor elements from the parent phase, thereby reducing proton conductivity. Although the dissolution state of sintering aids has not been clarified, the impact of local structural changes occurring due to dissolution on ion transport remains unknown. Previous studies have analyzed the dissolution state using X-ray diffraction (XRD) and scanning transmission electron microscope (STEM) through lattice constant changes.[45,46] However, owing to the low addition levels of sintering aids and complex interactions such as liquid-phase formation and lattice shrinkage, a definitive understanding of the dissolution state has not been achieved.

This study aimed to clarify the dissolution state of sintering aids and their mechanisms for promoting sinterability and influencing proton conduction. CuO was selected as a sintering aid and added to two types of proton-conducting oxides, $BaCe_{0.4}Zr_{0.4}Y_{0.1}Yb_{0.1}O_{3-\delta}$ (BCZYY441) and $BaCe_{0.7}Zr_{0.1}Y_{0.1}Yb_{0.1}O_{3-\delta}$ (BCZYY771). To investigate the reactivity of BCZYY441 with CuO in detail, diffusion couples between CuO and BCZYY441 were fabricated, and the effects of liquid-phase formation and CuO dissolution into the lattice on the promotion of sintering were evaluated. Additionally, the dissolution state of Cu^{2+} was analyzed using Raman and electron spin resonance (ESR) spectroscopy. Spectroscopic methods for structural analysis are sensitive to crystal symmetry and local configurations in the crystal structure, enabling more detailed structural analysis.[47] CuO was chosen for its efficacy as a sintering aid and because Cu^{2+} has an electron configuration ($3d^9$) that allows the analysis of the local structure through the hyperfine structure in ESR spectroscopy. The effects of Cu dissolution into the lattice on proton conduction were examined by measuring the proton concentration and proton transference number.

Experimental

Sample preparation

BCZYY441 was synthesized using a solid-state reaction. Raw powders of $BaCeO_3$ (99.95%, High Purity Chemicals), CeO_2 (99.9%, High Purity Chemicals), ZrO_2 (99.9%, High Purity Chemicals), Y_2O_3 (99.9%, High Purity Chemicals), and Yb_2O_3 (99.95%, Kanto Chemicals) were weighed in stoichiometric proportions and mixed in a planetary ball mill with stabilized zirconia pots and balls in heptane at 300 rpm for 3 h. After debinding, the powder was pressed into pellets at 200 MPa and sintered at 1600 °C for 10 h in alumina crucibles. The sintered pellets were pulverized again using a planetary ball mill at 300 rpm for 12 h to produce the BCZYY441 powder.

Diffusion couples were fabricated by re-sintering the BCZYY441 pellets at 1600 °C for 10 h in alumina crucibles. Prior to slurry deposition, the surface of BCZYY441 was polished using #320, #600, #1000, and #3000 abrasive papers, taking into account the preferential Ba deficiency at the surface. Subsequently, CuO slurry was applied to the polished surface. The slurry was prepared by mixing CuO (99.9%, High Purity Chemicals) with a solvent (Table S1) at a weight ratio of 3 : 1. The mixture was homogenized and defoamed at 2000 rpm for 1 min using a planetary rotation mixer (ARE-310, THINKY). After slurry application and debinding, the diffusion couple samples were heat treated at 900, 1000, and 1200 °C for 10 h at a heating rate of 5 °C min^{-1}. Cross-sections of the heat-treated samples were cut using a low-speed cutter and polished with a cross-section polisher (SM-09010, JEOL) at an acceleration voltage of 6.0 kV and an ion current of 0.130 mA for 10 h.

To analyze the dissolution state, BCZYY441 powder was mixed with 1 mol% CuO using a planetary ball mill at 200 rpm for 30 min, pressed under 200 MPa, and sintered at 1200 °C for 10 h. A control sample without CuO was prepared under the same conditions. Proton concentration was evaluated using $BaCe_{0.4}Zr_{0.4}Y_{0.1}Yb_{0.1}O_{3-\delta}$ provided by Toshiba Energy Systems & Solutions Corporation. The proton transference numbers were also measured for $BaCe_{0.4}Zr_{0.4}Y_{0.1}Yb_{0.1}O_{3-\delta}$, $BaCe_{0.7}Zr_{0.1}Y_{0.1}Yb_{0.1}O_{3-\delta}$, $Ba_{0.98}Ce_{0.4}Zr_{0.4}Y_{0.1}Yb_{0.1}Cu_{0.02}O_{3-\delta}$, and $BaCe_{0.68}Zr_{0.1}Y_{0.1}Yb_{0.1}$-$Cu_{0.02}O_{3-\delta}$ (KUSAKA RARE METAL).

Evaluation methods

The crystal structure was analyzed using XRD with Cu Kα radiation and transmission electron microscopy (TEM). Microstructural observations were performed using electron probe microanalyzer (EPMA, JXA-8530F, JEOL) and field-emission scanning electron microscopy (FE-SEM, JSM-IT800, JEOL). Chemical composition was measured by inductively coupled plasma mass spectrometry (ICP-MS). Local structural analyses were conducted on the cross sections of the prepared samples using Raman spectroscopy (HR-800, HORIBA) with a He–Ne laser source (wavelength: 632.8 nm). Density functional theory (DFT) calculations were used to characterize the observed vibrations using the Vienna *Ab initio* Simulation Package (VASP) code.[48] An orthorhombic *Imma* crystal structure model of $BaZrO_3$ consisting of 20 atoms, with lattice parameters of $a = 5.9788$ Å, $b = 6.0477$ Å, $c = 8.4205$ Å, was created. The exchange-correlation functional was the generalized gradient approximation (GGA-PBE). Using the relaxed model, displacement structures were generated using the Phonopy package and force calculations were performed using the finite difference method.[49,50] The cutoff energy was 500 eV, and the convergence criterion was set to 1×10^{-8} eV $Å^{-1}$ with $5 \times 4 \times 4$ *k*-point mesh.

For the local structural analysis of Cu^{2+}, ESR spectroscopy (JES-X330, JEOL) was used at the X-band frequency (9445 MHz). Mn, with $g_3 = 2.003$ and $g_4 = 1.981$, was used as the standard magnetic field marker. The proton concentration was evaluated using thermogravimetric analysis (TGA).[51] The samples were dried under vacuum at 800 °C for 5 h, and then gently compacted into pellets with a diameter of 5 mm using a uniaxial

press. They were first heated in dry N_2 to 900 °C without humidification, and then the atmosphere was switched to 0.0061 atm H_2O in N_2 and cooled to 300 °C at a rate of 10 °C min^{-1} with temperature steps of 100 °C. During the cooling process, isothermal holds were applied at 900, 800, 700, 600, and 500 °C for 90 min each, at 400 °C for 240 min, and at 300 °C for 360 min to ensure full hydration. Buoyancy correction was performed using data recorded for alumina as the reference material. The proton concentration was calculated from the weight gain, using eqn (1):

$$H_2O + V_O^{\cdot\cdot} + O_O^{\times} = 2OH_O^{\cdot} \quad (1)$$

The proton transference number was measured at 700 °C using the electromotive force (EMF) method under partial pressure gradient of water vapor, with N_2 gas flowing through both electrode chambers.[52–54] The water vapor partial pressure at one side of the electrode was fixed at $P^{I}_{H_2O} = 0.0121$ atm, while that at the opposite electrode was varied between $P^{II}_{H_2O} = 0.0419 - 0.308$ atm. Under conditions where the oxide ion transference number ($t_{O^{2-}}$) and proton transference number (t_{H^+}) can be considered constant regardless of chemical potentials, the electromotive force generated between the two electrodes can be described by eqn (2):

$$E = t_{O^{2-}} \frac{RT}{4F} \ln \frac{P^{II}_{O_2}}{P^{I}_{O_2}} - t_{H^+} \frac{RT}{2F} \ln \frac{P^{II}_{H_2}}{P^{I}_{H_2}} \quad (2)$$

Based on the equilibrium in eqn (3), the EMF can be expressed as a function of the partial pressures of water vapor and oxygen, as shown in eqn (4):

$$2H_2 + O_2 = 2H_2O \quad (3)$$

$$E = -t_{H^+} \frac{RT}{2F} \ln \frac{P^{II}_{H_2O}}{P^{I}_{H_2O}} + (t_{H^+} + t_{O^{2-}}) \frac{RT}{4F} \ln \frac{P^{II}_{O_2}}{P^{I}_{O_2}} \quad (4)$$

In this experiment, even though the same carrier gas (N_2) was used on both sides, differences in the water vapor partial pressure and minor leaks could cause small variations in the oxygen partial pressure. Although the resulting electromotive force is small compared with the difference in the water vapor partial pressure, it may still reflect these slight variations. Therefore, multiple points were taken, and the proton transference number was determined from the slope of the resulting plot (corresponding to the first term in eqn (4)). The slight offset at the origin (no pH_2O gradient) is attributed to the small EMF contribution from the second term in eqn (4).

Results and discussion

Sintering behavior of CuO-added BCZYY441

To analyze the reactivity between CuO and BCZYY441 in detail and investigate the sintering promotion effect due to solid solution and liquid phase formation, diffusion couples were prepared and heat-treated in the temperature range 900–1200 °C. The chemical composition of BCZYY441 after reactive sintering and re-sintering of the diffusion couples was analyzed by ICP-MS, as shown in Table S2. Although the compositions exhibited Ba deficiency, there was no significant difference between the first and second sintering. Fig. S1 shows the microstructure of BCZYY441 after reactive sintering and re-sintering for diffusion couples at 1600 °C for 10 h prior to CuO slurry deposition; both samples exhibited low relative densities of 79.2% and 84.7%. Fig. 1(a) shows the cross-sectional images of the diffusion couple of CuO and BCZYY441 heat-treated at 900, 1000, and 1200 °C for 10 h. In the sample heat-treated at 900 °C, only the region up to 90 μm from the surface turned black, whereas the samples heat-treated at 1000 °C and 1200 °C exhibited black coloration throughout the cross-section. For the sample heat-treated at 900 °C, the Cu distribution was analyzed by EPMA line analysis, as shown in Fig. 1(b). The presence of Cu was detected in the black-colored surface region of 90 μm, while the signal intensity beyond this region dropped to the background level. This indicates that the black coloration in the region up to 90 μm from the surface is due to the diffusion of Cu into BCZYY441.

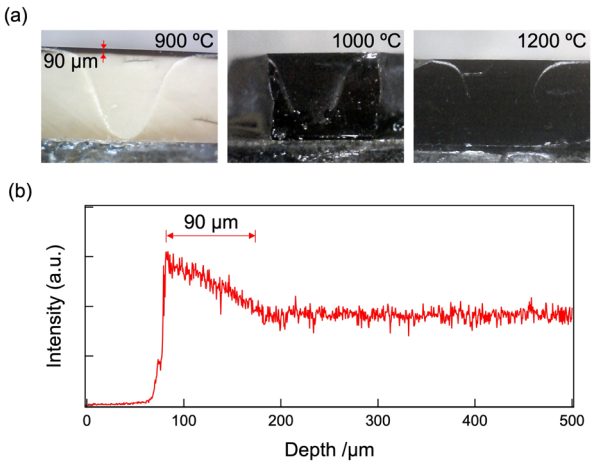

Fig. 1 (a) Cross-sectional images of diffusion couples between CuO and BCZYY441 heat-treated at 900, 1000, and 1200 °C for 10 h. (b) EPMA line analysis of Cu across the cross-section of the diffusion couple heat-treated at 900 °C.

The X-ray powder diffraction patterns of the surface of the diffusion couple samples before and after heat treatment at 900, 1000, and 1200 °C are shown in Fig. 2. The crystal structure of BCZYY depends on the Ce/Zr content and temperature, and varies depending on the preparation method and calcination temperature, even with the same nominal composition.[55] In this study, BCZYY441 was assigned to orthorhombic *Imma* based on XRD, as well as detailed TEM diffraction analysis. As shown in Fig. S2, for $BaCe_{0.5}Zr_{0.5}O_3$(BCZ55), diffraction spots with a *d*-spacing of 5.25 nm were observed, which correspond to the $(10\bar{1})$ reflection of the orthorhombic phase and are not present in the cubic structure. Based on this analysis, BCZYY441, which host is BCZ55, is also assumed to have the orthorhombic structure. The sample heat treated at 900 °C exhibited only peaks corresponding to orthorhombic perovskite, with no secondary phases detected, suggesting that no reaction

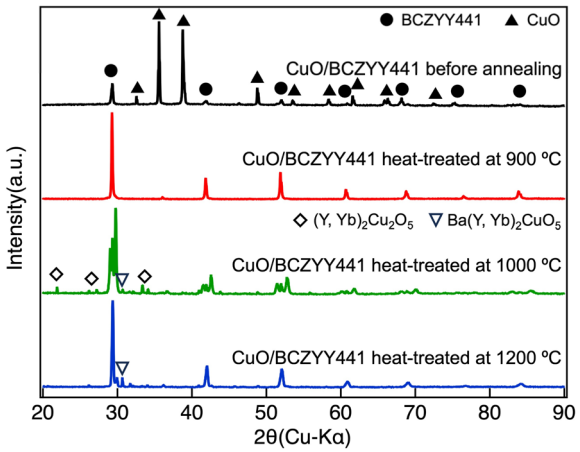

Fig. 2 X-ray powder diffraction patterns of diffusion couples between CuO and BCZYY441 before and after heat-treating at 900, 1000, and 1200 °C for 10 h.

occurred between CuO and BCZYY441 at this temperature. In contrast, the samples heat-treated at 1000 °C and 1200 °C exhibited peaks corresponding to orthorhombic perovskite as well as additional peaks attributed to $(Y,Yb)_2Cu_2O_5$ and $Ba(Y,Yb)_2CuO_5$. Considering that the eutectic point of the BaY_2CuO_5-CuO system is 967 °C and that of the $Y_2Cu_2O_5$-CuO system is 1048 °C, the formation of a liquid phase is suggested at heat-treatment temperatures above 1000 °C.[56]

For the diffusion couple samples, heat treatment at 900 °C resulted only in Cu dissolution into BCZYY441, whereas the formation of a liquid phase was observed above 1000 °C, as indicated by the presence of a low-melting secondary phase. To compare the sintering effects induced by Cu dissolution into the lattice and liquid phase formation, cross-sectional secondary electron images near the surface of the samples heat-treated at 900, 1000, and 1200 °C are shown in Fig. 3(a), and a schematic of the sintering mechanism is shown in Fig. 3(b). The sample heat treated at 900 °C exhibited a porous microstructure, whereas the samples heat treated at 1000 °C and above, where a liquid phase was formed, showed significant densification. EDS maps of each sample are shown in Fig. S3. The sample heat-treated at 900 °C exhibited little segregation, while samples heat-treated at 1000 °C and above showed segregation of Y, Yb, and Cu, which is likely attributable to secondary phases such as $(Y,Yb)_2Cu_2O_5$ and $Ba(Y,Yb)_2CuO_5$ observed in the XRD results. Additionally, the porosity at various depths for the 900 °C heat-treated diffusion couple sample was determined by binarizing the secondary electron images, as shown in Fig. S4. No significant change in porosity (4–6%) was observed between the Cu-diffused 90 μm region and the region beyond it. These results suggest that the sintering enhancement effect observed with the addition of CuO is primarily attributable to liquid-phase formation.

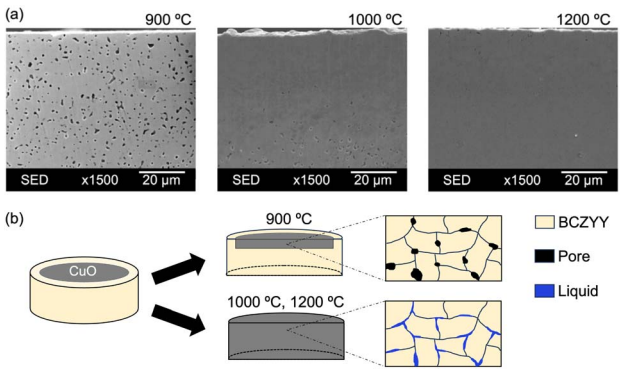

Fig. 3 (a) Secondary electron images of diffusion couples between CuO and BCZYY441 heat-treated at 900, 1000, and 1200 °C for 10 h. (b) Schematic diagram of diffusion couple and sintering mechanism.

Spectroscopic analysis of dissolution of Cu

Han *et al.* reported that Ni in BZY dissolves into interstitial sites adjacent to Ba, resulting in liquid-phase formation.[40,57] However, there are reports that sintering aids dissolve into the B-site, and no consensus has been reached regarding the dissolution site.[37,58] Therefore, Raman and ESR spectroscopy were used to analyze the detailed states of Cu dissolution.

First, diffusion couple sample heat-treated at 900 °C, where Cu was observed to dissolve only within the top 90 μm of the surface, was analyzed. In this region, as shown by EDS compositional analysis in Table S3, approximately 2.5 mol% of Cu was dissolved. Fig. 4(a) shows the Raman measurement point on the cross-section of the diffusion-coupled sample near the surface, and the corresponding Raman spectra at each point are shown in Fig. 4(b). Among the measurement points, the red, yellow, and green points represent the ones where Cu was dissolved, whereas the blue and purple points denote the areas where Cu was not dissolved. In cubic perovskites, there are no primary Raman-active vibrational modes. However, it is well known that local symmetry lowering can lead to the appearance of Raman peak, even in phases where Raman activity is nominally forbidden. In orthorhombic perovskites with reduced symmetry, 12 primary Raman modes exist, as expressed by eqn (5).

$$\Gamma_{\mathrm{Raman}} = 3A_g + 2B_{1g} + 3B_{2g} + 4B_{3g} \quad (5)$$

From the literature, the vibrational modes were analyzed.[59–62] In regions without Cu dissolution, spectra consistent with previous literature were obtained: a broad peak around 200 cm^{-1} corresponding to the Ba displacement mode against oxygen octahedra, peaks at 360 cm^{-1} and 395 cm^{-1} corresponding to out-of-plane displacements of B-site cations relative to in-plane oxygen, a peak at 460 cm^{-1} attributed to the rotation mode of the oxygen octahedra, and a peak at 690 cm^{-1} corresponding to the symmetric stretching vibrations of dopants and oxygen ions. In contrast, a specific peak was observed at 565 cm^{-1} in the regions where Cu was dissolved. To further investigate this specific peak, we examined the Raman spectra of BCZYY441, BCZYY711, and 5 mol% CuO-added BCZYY441 and BCZYY711, as shown in Fig. S5. In the CuO-added samples, peaks at 550 cm^{-1} for BCZYY711 and

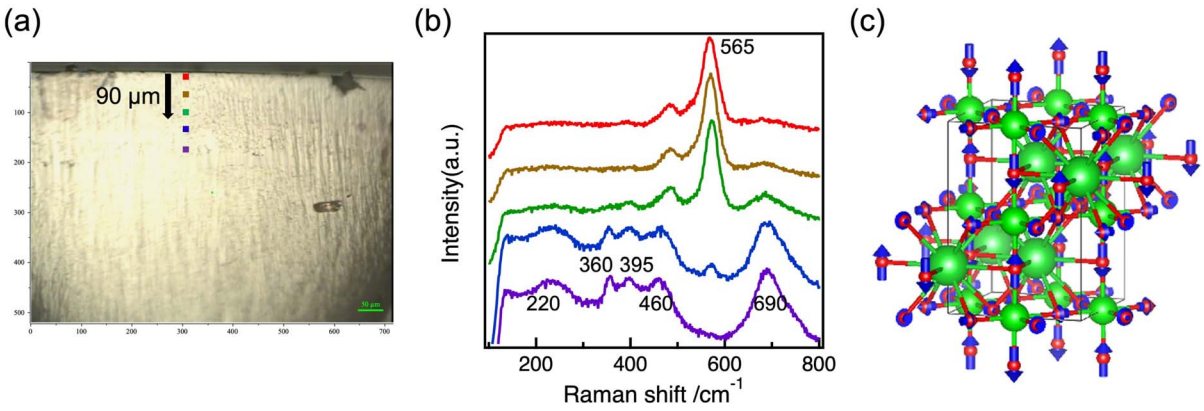

Fig. 4 (a) Raman measurement points for diffusion couples between CuO and BCZYY441 heat-treated at 900 °C. (b) Raman spectra at each point. (c) Vibrational mode of orthorhombic $BaZrO_3$ at 502 cm^{-1}.

565 cm^{-1} for BCZYY441 were observed. The shift to a lower wavenumber in BCZYY711 is likely due to its higher Ce content and larger lattice size, suggesting that the observed peak originates from BCZYY rather than from secondary phases. To assign this peak to a simplified model, we performed DFT calculations using orthorhombic $BaZrO_3$ (Table S4) even though $BaZrO_3$ itself is cubic. This model was selected based on the orthorhombic crystal structure of BCZYY441 and the observation that the peak becomes more pronounced with increasing Zr content. Based on this calculation, the vibrational mode at 565 cm^{-1}, observed only in the Cu-dissolved regions, is considered to correspond to the vibrational mode at 502 cm^{-1} calculated using DFT. As shown in Fig. 4(c), this vibrational mode involves the Jahn–Teller-like distortions of the oxygen octahedra. Previous studies on orthorhombic perovskite $BaZrO_3$ have also reported a Jahn–Teller-like vibrational mode at 535 cm^{-1}.[63] The observed peak at 565 cm^{-1} in the Cu-dissolved regions is likely enhanced due to the increased distortion of oxygen octahedra around Cu, resulting in greater polarization changes for this vibrational mode.

Although Raman spectroscopy suggested significant local structural changes due to Cu dissolution into the lattice, the local structure around Cu was further analyzed in detail using ESR spectroscopy. Cu^{2+}, with a nuclear spin $I_{Cu} = 3/2$, exhibits hyperfine splitting into four peaks due to interactions with the electron spin. Additionally, Cu^{2+}, with an electronic configuration of d^9, usually has five degenerate orbitals that split under a crystal field, as shown in Fig. 5(a). In an octahedral crystal field elongated along the axial direction, the g-values are given by eqn (6) and (7).

$$g_{\parallel} = g_e - \frac{8\lambda}{\Delta_0} \tag{6}$$

$$g_{\perp} = g_e - \frac{2\lambda}{\Delta_1} \tag{7}$$

where g_e is the g-value of a free electron, λ is the spin–orbit coupling constant, and Δ_0 and Δ_1 are the energy splitting widths in the elongated octahedral crystal field. As λ is negative for Cu^{2+}, the g-value relationship is $g_{\parallel} > g_{\perp} > g_e$ in an axially elongated octahedral crystal field.

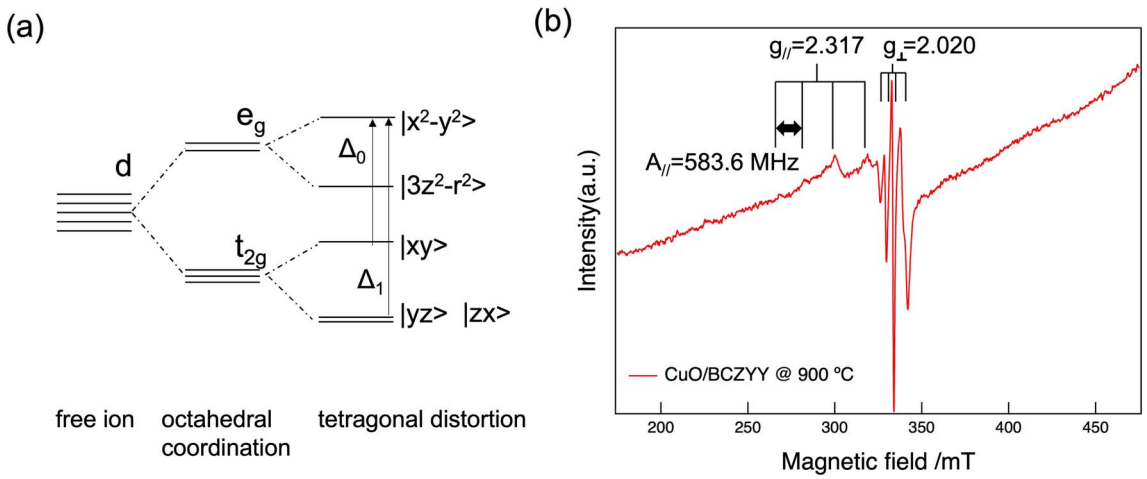

Fig. 5 (a) Schematic representation of orbital energy level of Cu^{2+} in a crystal field with octahedral symmetry and tetragonal distortion. (b) ESR spectra of the diffusion couples heat-treated at 900 °C.

Fig. 5(b) shows the ESR spectrum of the diffusion couple sample heat-treated at 900 °C, measured over the range of 175–475 mT. Hyperfine splitting into four peaks was observed on both the low and high magnetic field sides, indicating that the signals originated from unpaired electrons surrounding dissolved Cu^{2+}. Furthermore, anisotropy was observed, and the *g*-values were $g_{\parallel} = 2.317$ and $g_{\perp/} = 2.020$. This relationship suggests that Cu^{2+} occupies the x^2–y^2 orbital as the ground state, indicating that Cu is in an axially elongated octahedral position or planar four-coordinate interstitial site.

The coordination number of oxygen around Cu^{2+} can be evaluated using the hyperfine constant (*A*-value) and *g*-value, which depend on the degree of unpaired electron delocalization from Cu^{2+} to the nearby O^{2-}. As the number of coordinated oxygen atoms increased and the spin density on Cu^{2+} decreased, the spin–orbit coupling constant and *A*-value decreased. In Fig. 5(b), the *g*- and *A*-values are $g_{\parallel} = 2.317$ and $A_{\parallel} = 583.6$ MHz, respectively. Using the linear relationship between the *g*-value and *A*-value determined by Eichel *et al.* for the defect structures around Cu^{2+} in metal oxides, it was suggested that Cu^{2+} exists in a fourfold-coordinated environment in BCZYY, as shown in Fig. 6.[64]

Based on these results, the following two possible defect structures around Cu^{2+} were considered.

(I) Cu^{2+} was incorporated into site B, which was accompanied by two oxygen vacancies.

(II) Cu^{2+} is incorporated into an interstitial site adjacent to the A site.

In the first case, Cu^{2+} (a divalent acceptor) is typically accompanied by only one oxygen vacancy. Thus, the presence of two oxygen vacancies would require compensation by oxygen vacancies introduced by the Y or Yb dopants. Thus, ESR spectroscopy was conducted on $BaCe_{0.5}Zr_{0.5}O_3$ (BCZ55) with the addition of 1 mol% CuO and sintered at 1200 °C, which contained no Y or Yb dopants. Fig. 7 shows the ESR spectra of BCZ55 and BCZYY441. Hyperfine splitting originating from Cu^{2+} was observed, and the *g* and *A*-value were $g_{\parallel} = 2.302$ and $A_{\parallel} = 547.7$ MHz, respectively. This suggests that even in BCZ55 with 1 mol% CuO, Cu^{2+} was coordinated with four oxygen ions. Based on this analysis, the defect structure around Cu^{2+} corresponds to case II, and Cu^{2+} was incorporated at the interstitial site. This finding supports Han's claim that Ni is incorporated at interstitial sites in the trivalent state. However, it is still possible that Cu substitutes at the B-site, accompanied by two oxygen vacancies, owing to its strong interaction with the oxygen vacancies. Nevertheless, as shown in the ICP-MS results in Table S5 for BCZYY441 after re-sintering at 1600 °C and BCZYY441 with the addition of 3 mol% CuO and sintering at 1200 °C, the addition of CuO clearly increased Ba deficiency. This is more plausibly explained by the incorporation of Cu into the interstitial sites rather than by B-site substitution. Moreover, the stability of interstitial Cu incorporation depends on the level of Ba deficiency. As the BCZYY441 used in this study was already Ba-deficient, we prepared a Ba-stoichiometric sample by sintering on a zirconia plate, because sintering in alumina crucibles likely causes Ba loss due to secondary phase formation.[39] The lattice parameters and volumes of BCZYY441 sintered on a zirconia plate and alumina crucible were calculated using XRD after vacuum heat treatment at 800 °C for 5 h (Table S6). Compared to Ba-stoichiometric BCZYY441 sintered on a zirconia plate, Ba-deficient BCZYY441 sintered in an alumina crucible exhibited lattice contraction, which is consistent with previous reported results.[65,66] As shown in the ICP-MS results in Table S7, the sample sintered at 1600 °C on a zirconia plate exhibited a nearly stoichiometric composition.

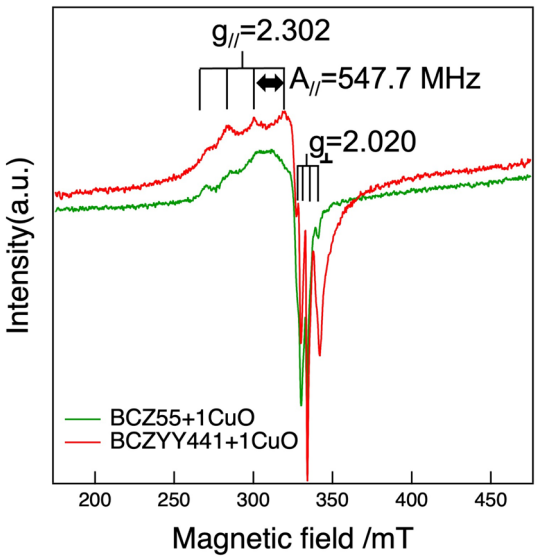

Fig. 7 ESR spectra of BCZYY441 with 1 mol% CuO and BCZ55 with 1 mol% CuO.

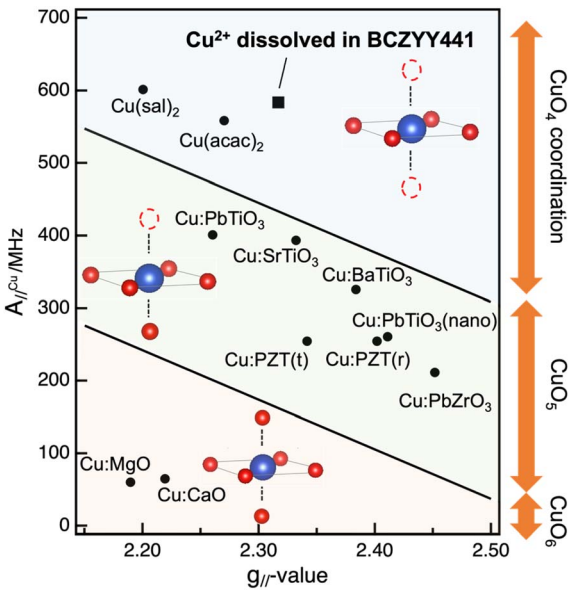

Fig. 6 Linear dependencies of $g_{\parallel,zz}$ *vs.*[63] $A_{\parallel Cu,zz}$ spin-Hamiltonian parameters for varying the oxygen coordination of Cu^{2+} centers with the indicated defect structure, in which the ESR data of diffusion couple heat-treated at 900 °C, along with those of Cu in various oxides cited from Eichel *et al.*, are plotted.[64]

However, after the addition of 3 mol% CuO and sintering at 1200 °C on a zirconia plate, a significant Ba deficiency was observed. This was likely due to the interstitial incorporation of Cu, as described above. Fig. S6 shows the ESR spectrum of BCZYY441 sintered on a zirconia plate with 3 mol% CuO. Hyperfine splitting originating from Cu^{2+} was observed, with $g_{\|} = 2.302$ and $A_{\|} = 547.7$ MHz. Using the linear relationship between *g*-value and *A*-value as shown in Fig. 6, it was confirmed that Cu was coordinated by four oxygen ions, suggesting that even in Ba-stoichiometric BCZYY441, the addition of CuO may induce Ba loss due to the interstitial incorporation of Cu. This is consistent with the study by Polfus *et al.*, which reported that interstitial Ni strongly associates with Ba vacancies.[67] Although the ionic radius of Cu is slightly larger than that of Ni, a similar defect association, *i.e.*, $(Cu_i v_{Ba})^{\times}$, is considered to occur.

In this study, it was suggested that Cu^{2+} is incorporated at the interstitial sites, accompanied by Ba vacancies, to maintain electrical neutrality. Examination of the sintering effect using diffusion-coupled samples indicated that the formation of a liquid phase is essential for sintering enhancement. Furthermore, Ba segregated at the grain boundaries, as suggested by ESR spectroscopy, was considered to promote liquid-phase formation and advance densification.

Effect of Cu dissolution on proton conduction

The relationship between CuO dissolution into the lattice and proton conduction in BCZYY441 was analyzed using the proton concentration and proton transference number of BCZYY441 with CuO and sintered at 1200 °C for 10 h. The proton concentration was evaluated using thermogravimetric analysis, and the TGA curves of BCZYY441 with 0 to 5 mol% CuO addition are shown in Fig. S7. Fig. 8 shows the proton concentration per unit cell for each CuO addition. Similar to results from previous studies,[35] it was found that the addition of CuO negatively affected the proton concentration. This may be due to the reduction in the effective acceptor concentration caused by Cu^{2+} incorporation into interstitial sites in the lattice and the reduction in acceptor concentration due to the formation of $Ba(Y,Yb)_2CuO_5$. Even in the sample without CuO addition, the proton concentration was lower than the nominal acceptor concentration, likely because of acceptor substitution at the A-site caused by Ba deficiency. As shown in Fig. S8, the Ba-stoichiometric BCZYY441 sintered on a zirconia plate exhibited a proton concentration of 19.2 mol%, which is close to the theoretical value. In addition to the Toshiba powder, we also conducted TGA measurements using the same homemade BCZYY441 powder. The TGA curves and proton concentrations are shown in Fig. S9. At 300 °C, the proton concentration was 15.6 mol% for BCZYY441 without CuO and 13.7 mol% for BCZYY441 with 3 mol% CuO. These results indicate that the addition of CuO adversely affects proton uptake, consistent with the results obtained using the Toshiba powder.

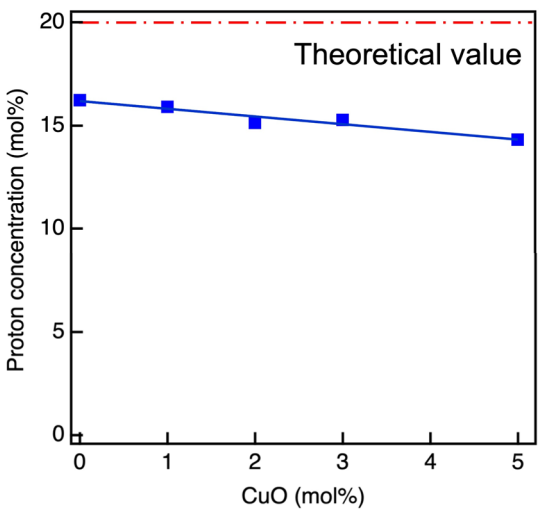

Fig. 8 Proton concentration of BCZYY441 as a function of CuO contents.

Fig. S10 shows the van't Hoff plots calculated using the nominal and effective acceptor concentrations. The mass action constant for the hydration reaction $K_{hydration}$ was calculated using eqn (11), which is derived from eqn (8), the oxygen site restriction (eqn (9)) and the electroneutrality condition (eqn (10)):

$$K = \frac{[OH_O^{\cdot}]^2}{[O_O^{\times}][V_O^{\cdot\cdot}]p(H_2O)} \quad (8)$$

$$[OH_O^{\cdot}] + [V_O^{\cdot\cdot}] + [O_O^{\times}] = 3 \quad (9)$$

$$2[V_O^{\cdot\cdot}] + [OH_O^{\cdot}] = S \quad (10)$$

$$K = \frac{4[OH_O^{\cdot}]^2}{(S - [OH_O^{\cdot}])(6 - S - [OH_O^{\cdot}])p(H_2O)} \quad (11)$$

The van't Hoff plots calculated using the nominal acceptor concentration showed a decreasing trend at lower temperatures, indicating that the maximum proton concentration was significantly lower than the nominal acceptor concentration. This suggests that Ba deficiency led to partial substitution of acceptors at the A-site. The hydration enthalpy and entropy were calculated using eqn (12), and were summarized in Table S8.

$$\ln K = -\frac{\Delta H^{\circ}}{RT} + \frac{\Delta S^{\circ}}{R} \quad (12)$$

The ΔH° values were in the range of −114 to −133 kJ mol^{-1}, and the ΔS° values were in the range of −127 to −146 J mol^{-1} K^{-1}. No clear trend was observed with respect to the amount of sintering aid.

The proton transference number was close to unity in the CuO-free samples but decreased to 0.4 for BCZYY711 and 0.2 for BCZYY441 with 2 mol% CuO (Fig. S11). Cu dissolution leads to decrease in proton concentration, indicating that less oxide ion vacancies participated in the hydration reaction. As a result, hole formation, as described by eqn (13), is expected to be facilitated.

$$O_2 + 2V_O^{\cdot} = 2O_O^{\times} + 4h^{\cdot} \quad (13)$$

It has been reported that incorporation of transition metals into the lattice increases the hole concentration, thereby reducing the proton transference number.[68,69]

As Cu incorporation occurs at temperatures lower than those at which CuO acts as a sintering aid, balancing the advancement of sintering and the suppression of Cu incorporation is challenging. Thus, it is necessary to develop processes to remove the incorporated sintering aid through post-treatments such as reduction heat treatment, or to explore novel sintering aids that form a liquid phase without incorporation into the lattice.

Conclusions

In this study, diffusion couples between BCZYY441 and CuO were fabricated, and their reactivity was analyzed in detail to clarify the sintering mechanism. Raman spectroscopy and ESR spectroscopy were used to investigate the local structure of the incorporated sintering aids.

Diffusion couple experiments revealed that Cu dissolution into the lattice alone has minimal sintering effects, and liquid-phase formation is critical for sintering. From the ESR spectroscopy results, it was seen that the incorporated Cu^{2+} exhibited fourfold oxygen coordination, indicating that Cu^{2+} occupied interstitial sites in the lattice. This suggests that defect compensation of Ba vacancies occurs, and the reaction between Ba expelled to the grain boundaries by Cu incorporation and the sintering aid facilitates liquid-phase formation, promoting densification. However, Cu incorporation significantly reduces the proton transference number, highlighting the necessity of processes to remove the incorporated sintering aid through post-treatment or alternatively, the exploration of novel sintering aids. The densification mechanism and detailed dissolution state elucidated in this study are expected to provide critical guidelines for the design and optimization of proton-conducting materials.

Author contributions

Y. U.: writing – original draft, methodology, investigation, validation, data curation, and visualization. H. K.: conceptualization, investigation, validation, and writing – review. S. K.: investigation and validation. N. O.: investigation, validation, and resources. A. I.: investigation, validation, writing – review and editing. I. O.: investigation and validation. H. T.: conceptualization, methodology, validation, project administration, resources, writing – review and editing, and supervision.

Conflicts of interest

The authors declare no conflict of interest.

Data availability

Data for this article, including ICP-MS, TEM, SEM, and EDS mapping images, Raman spectra, DFT-calculated vibrational modes, ESR spectra, XRD, TGA, and EMF measurements, are available at Tohoku University Research Data Lake – IZUMI at **https://nc.rdx.tohoku.ac.jp/s/Fp3F92g8x4pQfew**.

ICP-MS, TEM, SEM, and EDS mapping images, Raman spectra, DFT-calculated vibrational modes, ESR spectra, XRD, TGA, and EMF measurements. See DOI: **https://doi.org/10.1039/d5ta03169a**.

Acknowledgements

This work was supported in part by JSPS KAKENHI grant number 22H04914 and Council for Science, Technology and Innovation (CSTI), Cross-ministerial Strategic Innovation Promotion Program (SIP), the third period of SIP "smart energy management system" grant number JPJ012207 (Funding agency: JST). The authors thank Ms Y. Nakano and Dr T. Miyazaki for technical help with the ICP-MS and TEM analysis.

References

1 T. Nakamura, S. Mizunuma, Y. Kimura, Y. Mikami, K. Yamauchi, T. Kuroha, N. Taniguchi, Y. Tsuji, Y. Okuyama and K. Amezawa, *J. Mater. Chem. A*, 2018, **6**, 15771–15780.
2 T. Chen, Y. Jing, L. O. Anderson, K. Leonard, H. Matsumoto, N. Aluru and N. H. Perry, *J. Phys. Chem. C*, 2021, **125**, 26216–26228.
3 H. Takahashi, I. Oikawa and H. Takamura, *J. Phys. Chem. C*, 2018, **122**, 6501–6507.
4 I. Oikawa and H. Takamura, *Chem. Mater.*, 2015, **27**, 6660–6667.
5 S. Kamohara, A. Ishii, I. Oikawa and H. Takamura, *ACS Appl. Mater. Interfaces*, 2024, **16**, 52339–52348.
6 H. Iwahara, T. Esaka, H. Uchida and N. Maeda, *Solid State Ionics*, 1981, **3–4**, 359–363.
7 K. Saito and M. Yashima, *Nat. Commun.*, 2023, **14**, 7466.
8 H. Kim, A. Jang, S. Choi, W. Jung and S. Chung, *Angew. Chem., Int. Ed.*, 2016, **55**, 13499–13503.
9 H. Kawamori, I. Oikawa and H. Takamura, *Chem. Mater.*, 2021, **33**, 5935–5942.
10 A. Ishii, D. Kume, S. Nakayasu, I. Oikawa, H. Matsumoto, H. Kato and H. Takamura, *Mater. Adv.*, 2024, **5**, 1531–1539.
11 H. Takahashi, I. Yashima, K. Amezawa, K. Eguchi, H. Matsumoto, H. Takamura and S. Yamaguchi, *Chem. Mater.*, 2017, **29**, 1518–1526.
12 T. Hibino, K. Mizutani, T. Yajima and H. Iwahara, *Solid State Ionics*, 1992, **57**, 303–306.
13 M. Scholten, J. Schoonman, J. Vanmiltenburg and H. Oonk, *Solid State Ionics*, 1993, **61**, 83–91.
14 K. Kreuer, E. Schonherr and J. Maier, *Solid State Ionics*, 1994, **70–71**, 278–284.
15 L. Yang, S. Wang, K. Blinn, M. Liu, Z. Liu, Z. Cheng and M. Liu, *Science*, 2009, **326**, 126–129.
16 S. Choi, T. C. Davenport and S. M. Haile, *Energy Environ. Sci.*, 2019, **12**, 206–215.
17 Y.-D. Kim, I.-H. Kim, C. Meisel, C. Herradón, P. W. Rand, J. Yang, H. S. Kim, N. P. Sullivan and R. O'Hayre, *J. Phys. Energy*, 2024, **6**, 035004.

18 K. D. Kreuer, *Solid State Ionics*, 1999, **125**, 285–302.
19 H. Guo, Y. Li, L. Jiang, Y. Sha, S. Guo and D. Han, *J. Mater. Chem. A*, 2024, **10**, 1039.
20 D. Han, K. Shinoda, S. Sato, M. Majima and T. Uda, *J. Mater. Chem. A*, 2015, **3**, 1243–1250.
21 N. Nasani, D. Ramasamy, S. Mikhalev, A. V. Kovalevsky and D. P. Fagg, *J. Power Sources*, 2015, **278**, 582–589.
22 J. Gao, Y. Meng, J. H. Duffy and K. S. Brinkman, *Adv. Energy Sustainability Res.*, 2021, **2**, 2100098.
23 Z. Zhao, J. Gao, Y. Meng, K. S. Brinkman and J. Tong, *Ceram. Int.*, 2021, **47**, 11313–11319.
24 Z. Liu, Y. Song, X. Xiong, Y. Zhang, J. Cui, J. Zhu, L. Li, J. Zhou, C. Zhou, Z. Hu, G. Kim, F. Ciucci, Z. Shao, J.-Q. Wang and L. Zhang, *Nat. Commun.*, 2023, **14**, 7984.
25 P. Babilo and S. M. Haile, *J. Am. Ceram. Soc.*, 2005, **88**, 2362–2368.
26 J. Wallis, L. Urban, C. Grimmer, W. Bodnar, R. Zimmermann, S. Ricote, K.-D. Weltmann, E. Burkel and A. Kruth, *Solid State Ionics*, 2020, **345**, 115118.
27 P. Castellani, E. Quarez, C. Nicollet, O. Joubert, N. Gautier, P. Pers, G. Taillades and A. Le Gal La Salle, *Int. J. Hydrogen Energy*, 2024, **54**, 1343–1356.
28 P. Hu, K. Gui, W. Hong, X. Zhang and S. Dong, *J. Eur. Ceram. Soc.*, 2017, **37**, 2317–2324.
29 J. N. Ebert, D. Jennings, O. Guillon and W. Rheinheimer, *Scr. Mater.*, 2025, **256**, 116414.
30 T. Zhou, H. Huang, Y. Meng, J. Conrad, M. Zou, Z. Zhao, K. S. Brinkman and J. Tong, *ACS Energy Lett.*, 2024, **9**, 4557–4563.
31 S. Mu, Z. Zhao, H. Huang, J. Lei, F. Peng, H. Xiao, K. S. Brinkman and J. Tong, *Electrochem. Soc. Interface*, 2020, **29**, 67–73.
32 A. Ishii, H. Ishijima, K. Kobayashi, I. Oikawa and H. Takamura, *Acta Mater.*, 2022, **224**, 117529.
33 R. Wang, G. Y. Lau, D. Ding, T. Zhu and M. C. Tucker, *Int. J. Hydrogen Energy*, 2019, **44**, 13768–13776.
34 L. K. Foong, B. H. Jume and C. Xu, *Ceram. Int.*, 2020, **46**, 28316–28323.
35 J. Tong, D. Clark, M. Hoban and R. O'Hayre, *Solid State Ionics*, 2010, **181**, 496–503.
36 S. Tao and J. T. S. Irvine, *J. Solid State Chem.*, 2007, **180**, 3493–3503.
37 S. Nikodemski, J. Tong and R. O'Hayre, *Solid State Ionics*, 2013, **253**, 201–210.
38 Y. Huang, R. Merkle and J. Maier, *J. Mater. Chem. A*, 2021, **9**, 14775–14785.
39 A. M. Dayaghi, J. M. Polfus, R. Strandbakke, A. Pokle, L. Almar, S. Escolástico, E. Vøllestad, J. M. Serra, R. Haugsrud and T. Norby, *Solid State Ionics*, 2023, **401**, 116355.
40 D. Han, K. Shinoda, S. Tsukimoto, H. Takeuchi, C. Hiraiwa, M. Majima and T. Uda, *J. Mater. Chem. A*, 2014, **2**, 12552.
41 H.-I. Ji, B.-K. Kim, J.-W. Son, K. J. Yoon and J.-H. Lee, *J. Power Sources*, 2021, **507**, 230296.
42 D. Han, S. Uemura, C. Hiraiwa, M. Majima and T. Uda, *ChemSusChem*, 2018, **11**, 4102–4113.
43 J. Tong, D. Clark, L. Bernau, M. Sanders and R. O'Hayre, *J. Mater. Chem.*, 2010, **20**, 6333.
44 X.-L. Lin, Z. U. D. Babar, Y. Gao, J.-T. Gao and C.-X. Li, *ACS Appl. Energy Mater.*, 2023, **6**, 4833–4843.
45 D. Gao and R. Guo, *J. Alloys Compd.*, 2010, **493**, 288–293.
46 S. Yang, S. Zhang, C. Sun, X. Ye and Z. Wen, *ACS Appl. Mater. Interfaces*, 2018, **10**, 42387–42396.
47 Y. Okazaki, A. Ishii, I. Oikawa and H. Takamura, *Small*, 2025, 2412830.
48 G. Kresse and J. Furthmüller, *Phys. Rev. B: Condens. Matter Mater. Phys.*, 1996, **54**, 11169–11186.
49 A. Togo, L. Chaput, T. Tadano and I. Tanaka, *J. Phys.: Condens. Matter*, 2023, **35**, 353001.
50 A. Togo, *J. Phys. Soc. Jpn.*, 2023, **92**, 012001.
51 K. Leonard, Y. Okuyama, M. E. Ivanova, W. A. Meulenberg and H. Matsumoto, *ChemElectroChem*, 2022, **9**, e202101663.
52 T. Norby, *Solid State Ionics*, 2000, **136–137**, 139–148.
53 A. Sharma, I. Suzuki, T. Ishiyama and T. Omata, *Phys. Chem. Chem. Phys.*, 2023, **25**, 18766–18774.
54 D. Sutija, *Solid State Ionics*, 1995, **77**, 167–174.
55 J. Jing, J. Pang, L. Chen, H. Zhang, Z. Lei and Z. Yang, *Chem. Eng. J.*, 2022, **429**, 132314.
56 W. Wong-Ng and L. P. Cook, *J. Res. Natl. Inst. Stand. Technol.*, 1998, **103**, 379–403.
57 J. M. Polfus, M.-L. Fontaine, A. Thøgersen, M. Riktor, T. Norby and R. Bredesen, *J. Mater. Chem. A*, 2016, **4**, 8105–8112.
58 K. Li, Y. Liang, J. Zhang, B. Yu and L. Jia, *Int. J. Hydrogen Energy*, 2024, **91**, 858–866.
59 E. Sediva and J. L. M. Rupp, *J. Mater. Chem. A*, 2023, **11**, 26752–26763.
60 D.-H. Gim, Y. Sur, Y. H. Lee, J. H. Lee, S. Moon, Y. S. Oh and K. H. Kim, *Materials*, 2022, **15**, 4286.
61 F. Giannici, M. Shirpour, A. Longo, A. Martorana, R. Merkle and J. Maier, *Chem. Mater.*, 2011, **23**, 2994–3002.
62 T. Scherban, R. Villeneuve, L. Abello and G. Lucazeau, *Solid State Ionics*, 1993, **61**, 93–98.
63 C. Toulouse, D. Amoroso, C. Xin, P. Veber, M. C. Hatnean, G. Balakrishnan, M. Maglione, P. Ghosez, J. Kreisel and M. Guennou, *Phys. Rev. B*, 2019, **100**, 134102.
64 R.-A. Eichel, M. D. Drahus, P. Jakes, E. Erünal, E. Erdem, S. K. S. Parashar, H. Kungl and M. J. Hoffmann, *Mol. Phys.*, 2009, **107**, 1981–1986.
65 Y. Guo, R. Ran, Z. Shao and S. Liu, *Int. J. Hydrogen Energy*, 2011, **36**, 8450–8460.
66 W. Yang, H. Zhou, L. Wang, Y. Li, Z. He, C. Han and L. Dai, *Int. J. Hydrogen Energy*, 2021, **46**, 10838–10849.
67 J. M. Polfus, M.-L. Fontaine, A. Thøgersen, M. Riktor, T. Norby and R. Bredesen, *J. Mater. Chem. A*, 2016, **4**, 8105–8112.
68 Y. Mikami, Y. Sekitani, K. Yamauchi, T. Kuroha and Y. Okuyama, *ACS Appl. Energy Mater.*, 2024, **7**, 1136–1148.
69 E. Kim, Y. Yamazaki, S. M. Haile and H.-I. Yoo, *Solid State Ionics*, 2015, **275**, 23–28.